Electronic Supplementary Material (ESI) for Energy & Environmental Science.

Supplementary information for

A sea-change: Manganese doped nickel/nickel oxide electrocatalysts for hydrogen generation from seawater

Xunyu Lu,* Jian Pan, Emma Lovell, Tze Hao Tan, Yun Hau Ng and Rose Amal*

Particles and Catalysis Research Group, School of Chemical Engineering, The University of New South Wales, Sydney, NSW 2052, Australia

Email: r.amal@unsw.edu.au
xunyu.lu@unsw.edu.au

List of Tables and Figures

Comment [RL]: Seems the figure order has not been correctly arranged. Figure S 28-30 comes before Figure S 22.

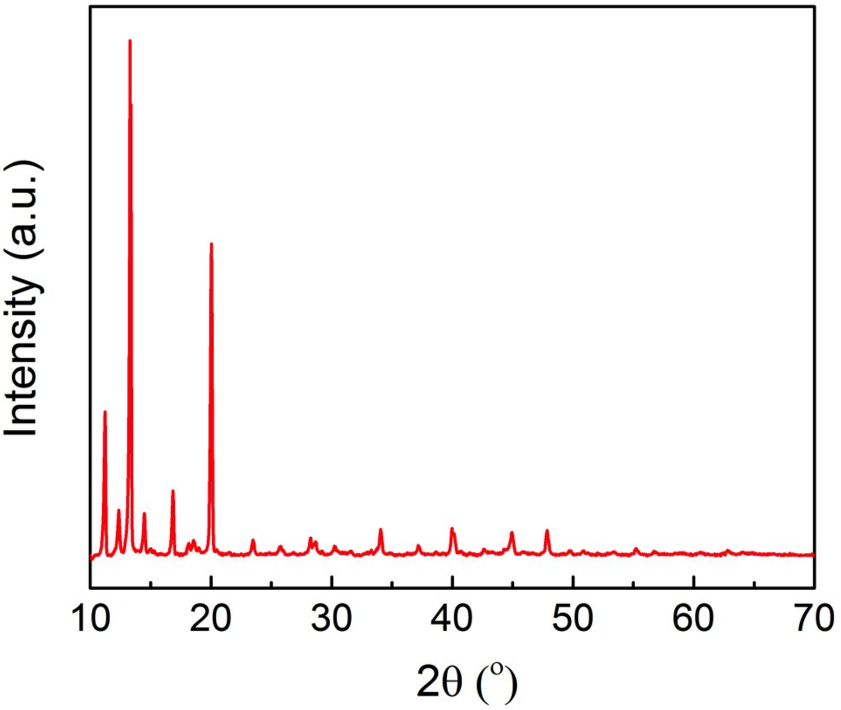

Figure S 1. XRD pattern of the Mn-MOF scratched off from Ni-F.

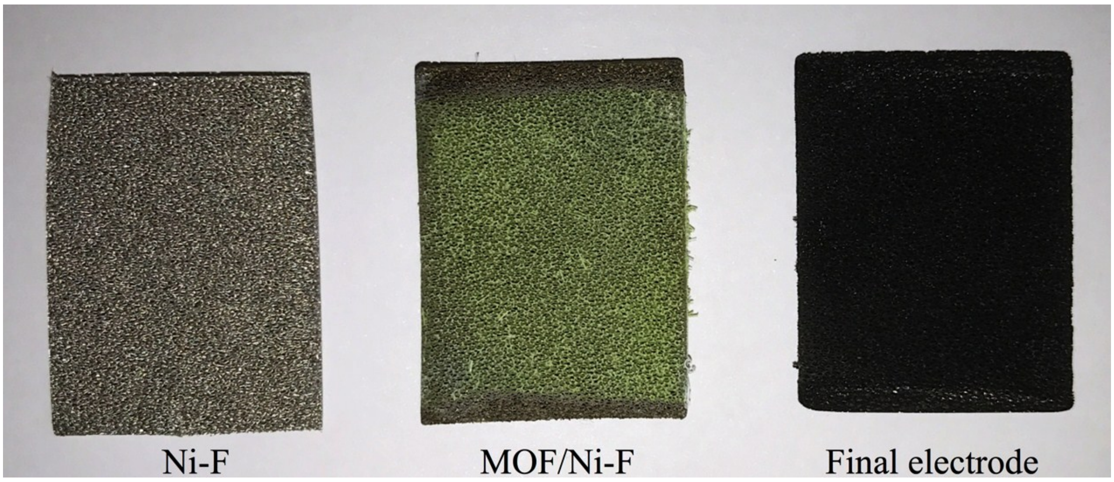

Figure S 2. Photos of the Ni-F, MOF/Ni-F and the final electrode, respectively.

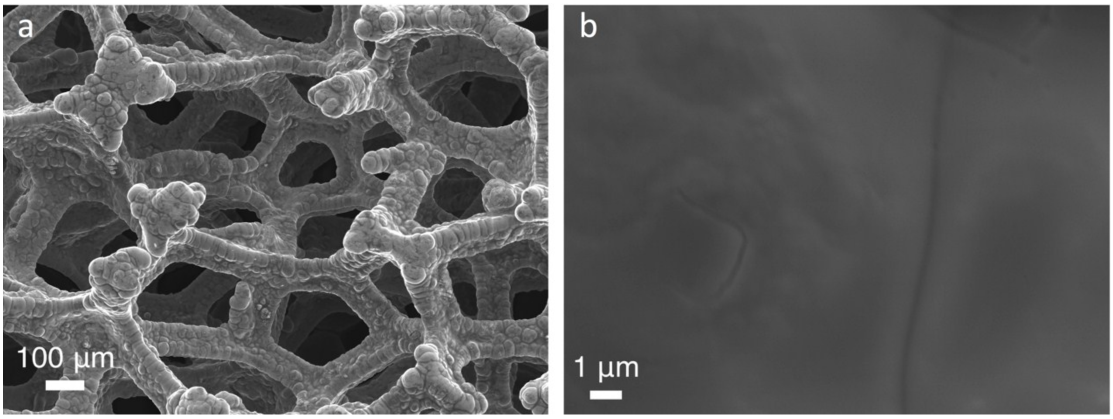

Figure S 3. SEM images of pure Ni-F under (a) low and (b) high magnifications.

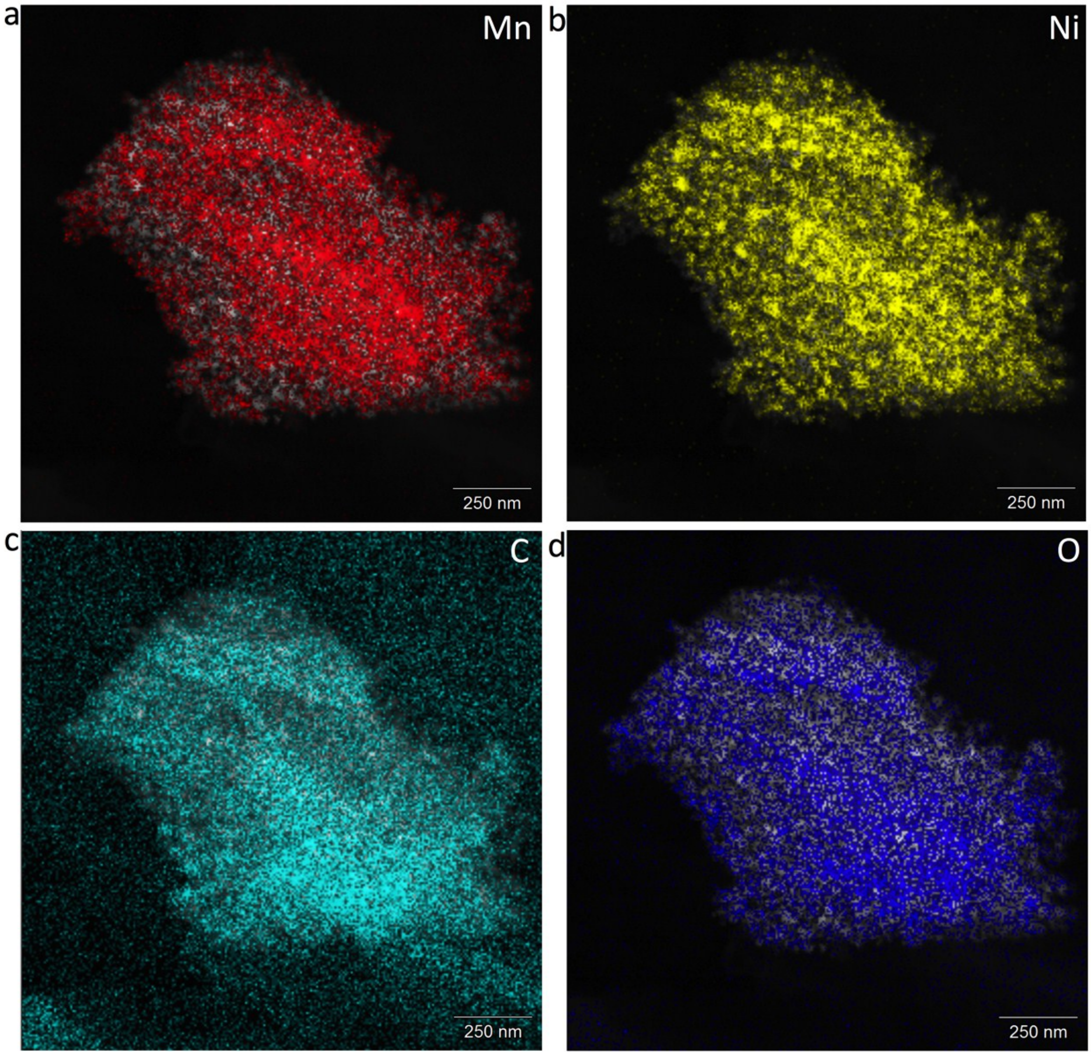

Figure S 4. Elemental mappings of the composite scratched off from the final electrode.

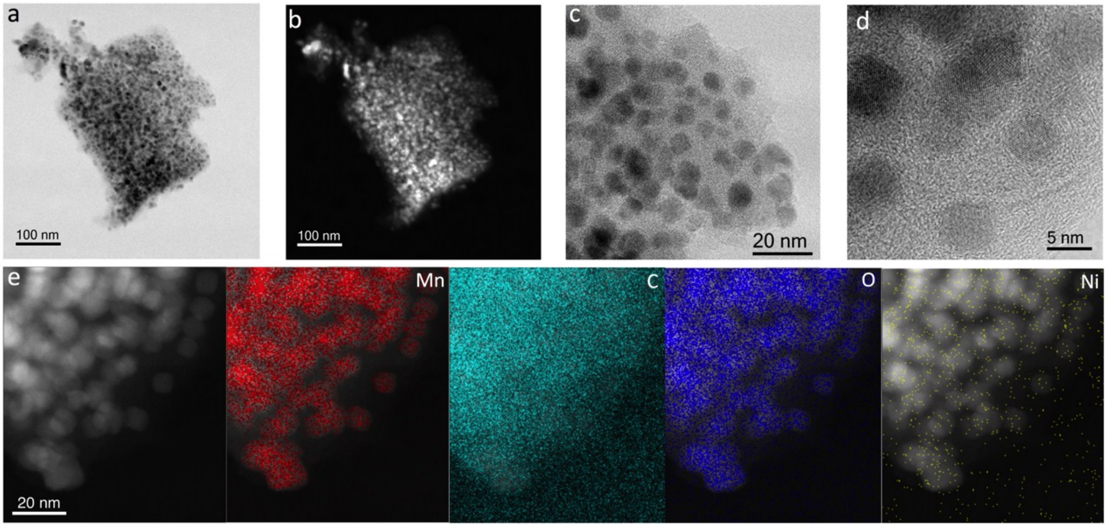

Figure S 5. (a) STEM image of the MnC powder derive from Mn-MOF. (b) The corresponding HADDF image of (a). (c) and (d) STEM images of MnC powder under higher magnifications. (e) The corresponding elemental mappings of the MnC powder.

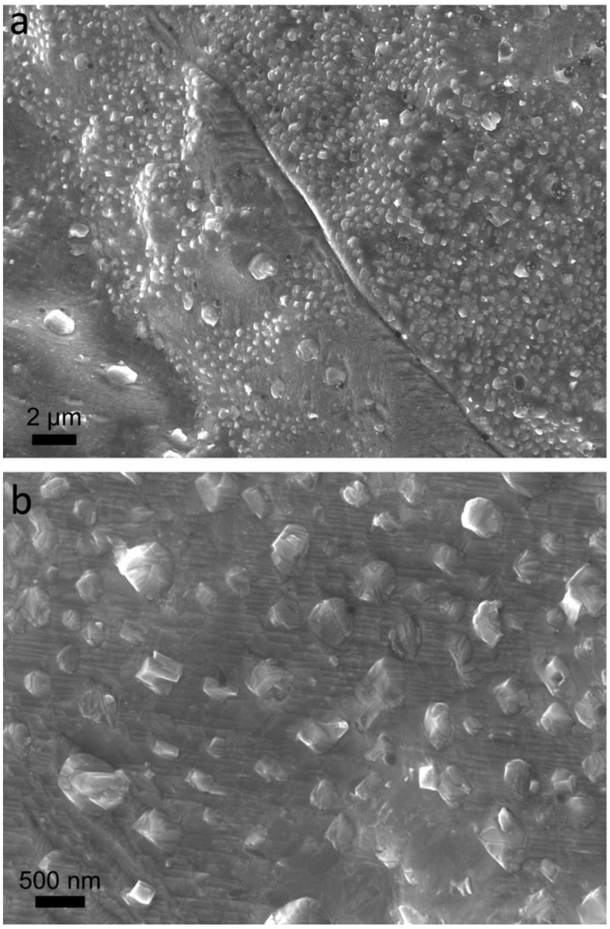

Figure S 6. SEM images of pure Ni-F after pyrolysis under different magnifications.

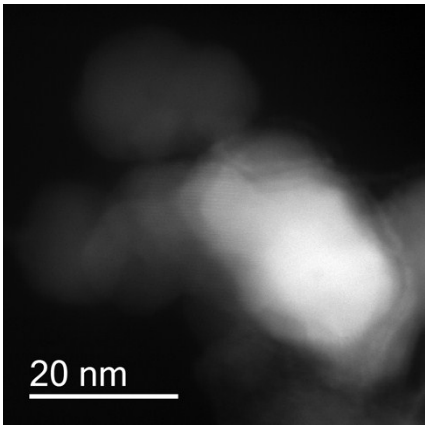

Figure S 7. High magnification HAADF-STEM image of the MnO-NiO-Ni composite.

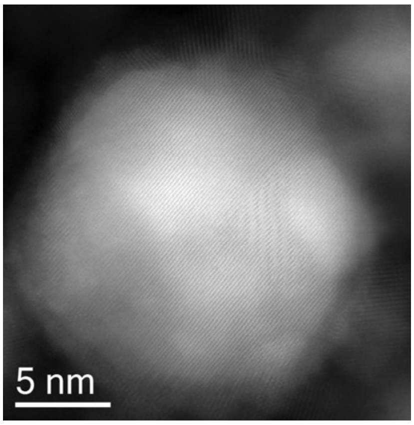

Figure S 8. HAADF-STEM image of an individual NiO-Ni hetero-structure.

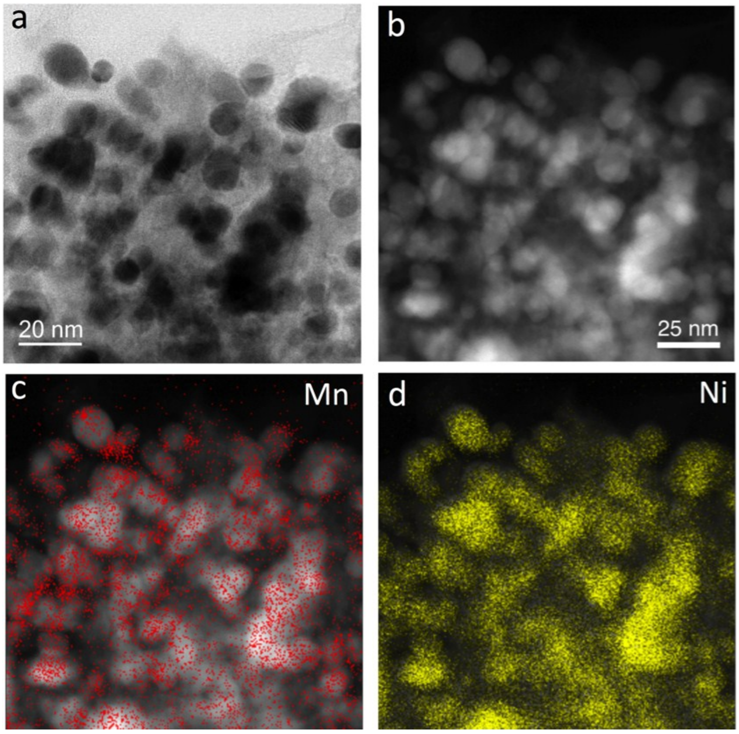

Figure S 9. (a) STEM image, (b) the corresponding HAADF image, (c) Mn element mapping and (d) Ni element mapping of MnO-NiO-Ni composites that have been scratched off from the electrode after 5 hours of HER in 1 M PB solution at an applied potential of -0.17 V.

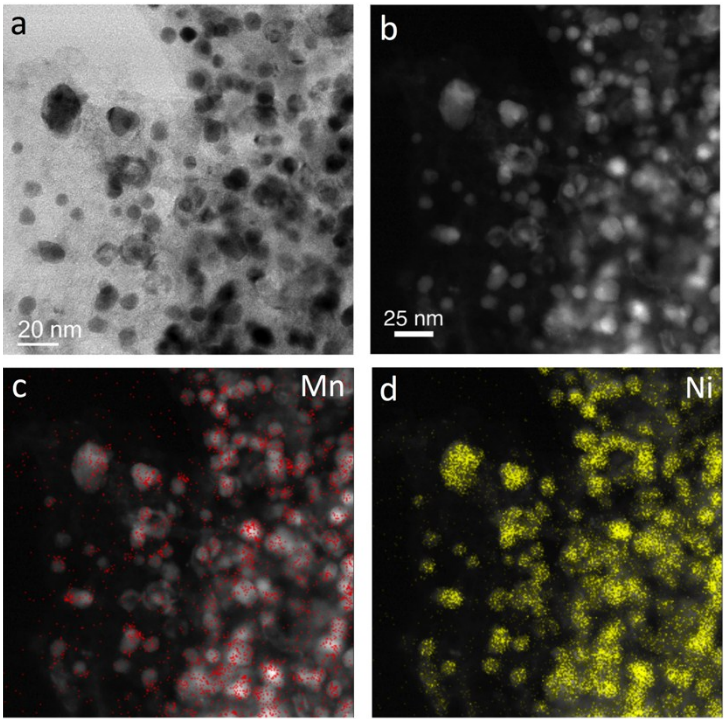

Figure S 10. (a) STEM image, (b) the corresponding HAADF image, (c) Mn element mapping and (d) Ni element mapping of MnO-NiO-Ni composites that have been scratched off from the electrode after 10 hours of HER in 1 M PB solution at an applied potential of -0.17 V.

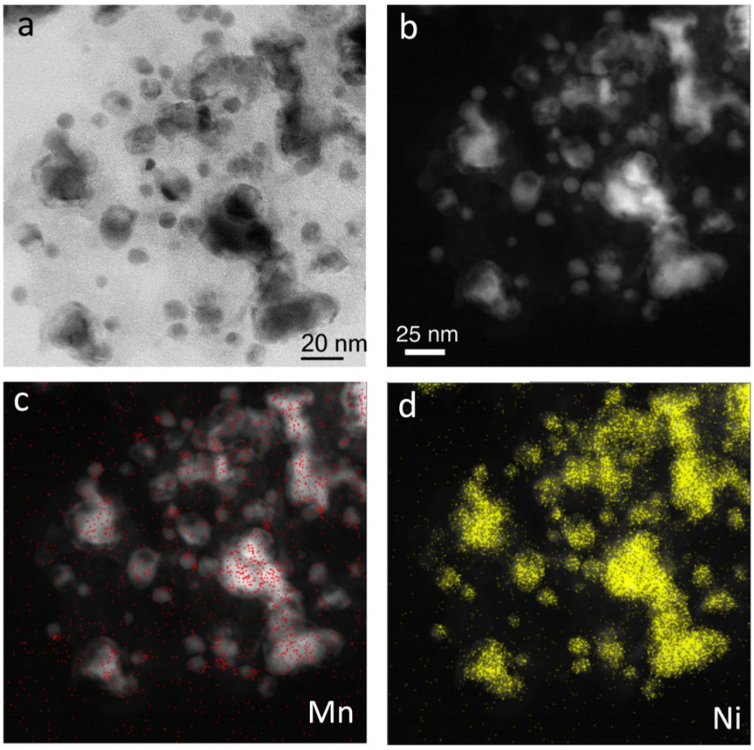

Figure S 11. (a) STEM image, (b) the corresponding HAADF image, (c) Mn element mapping and (d) Ni element mapping of MnO-NiO-Ni composites that have been scratched off from the electrode after 24 hours of HER in 1 M PB solution at an applied potential of -0.17 V.

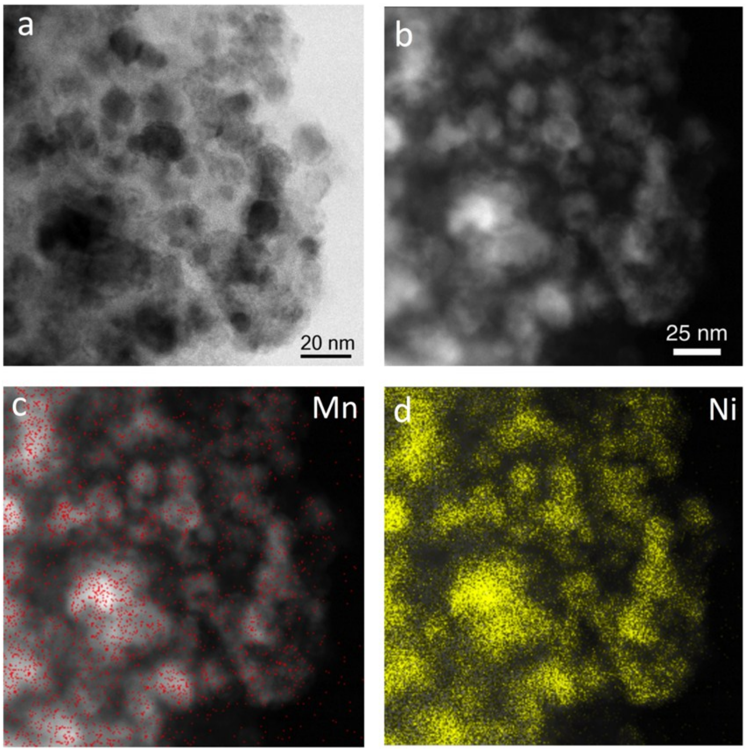

Figure S 12. (a) STEM image, (b) the corresponding HAADF image, (c) Mn element mapping and (d) Ni element mapping of MnO-NiO-Ni composites that have been scratched off from the electrode after 48 hours of HER in 1 M PB solution at an applied potential of -0.17 V.

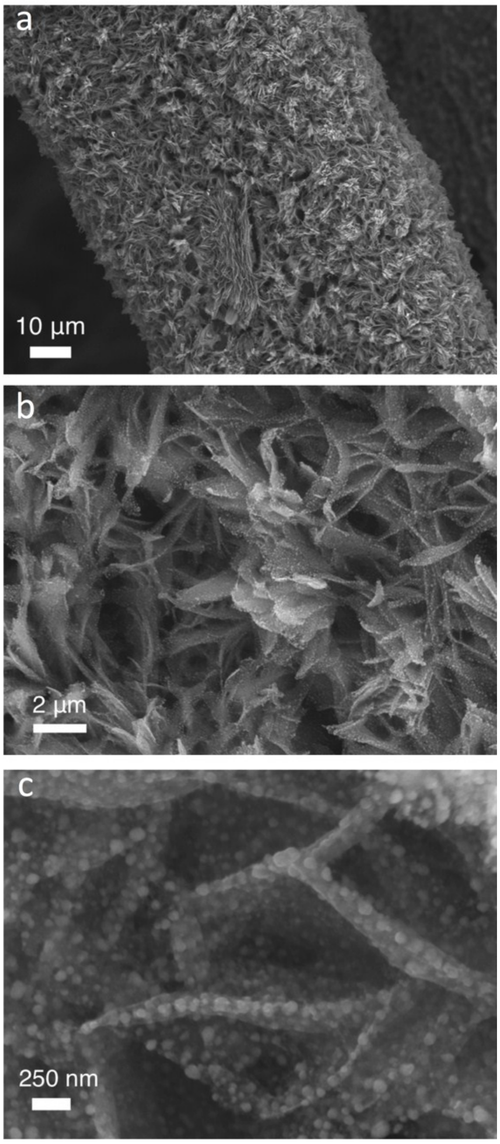

Figure S 13. SEM images of the MnO-NiO-Ni/Ni-F electrode after 48 hours of HER in 1 M PB solution at -0.17 V under different magnifications.

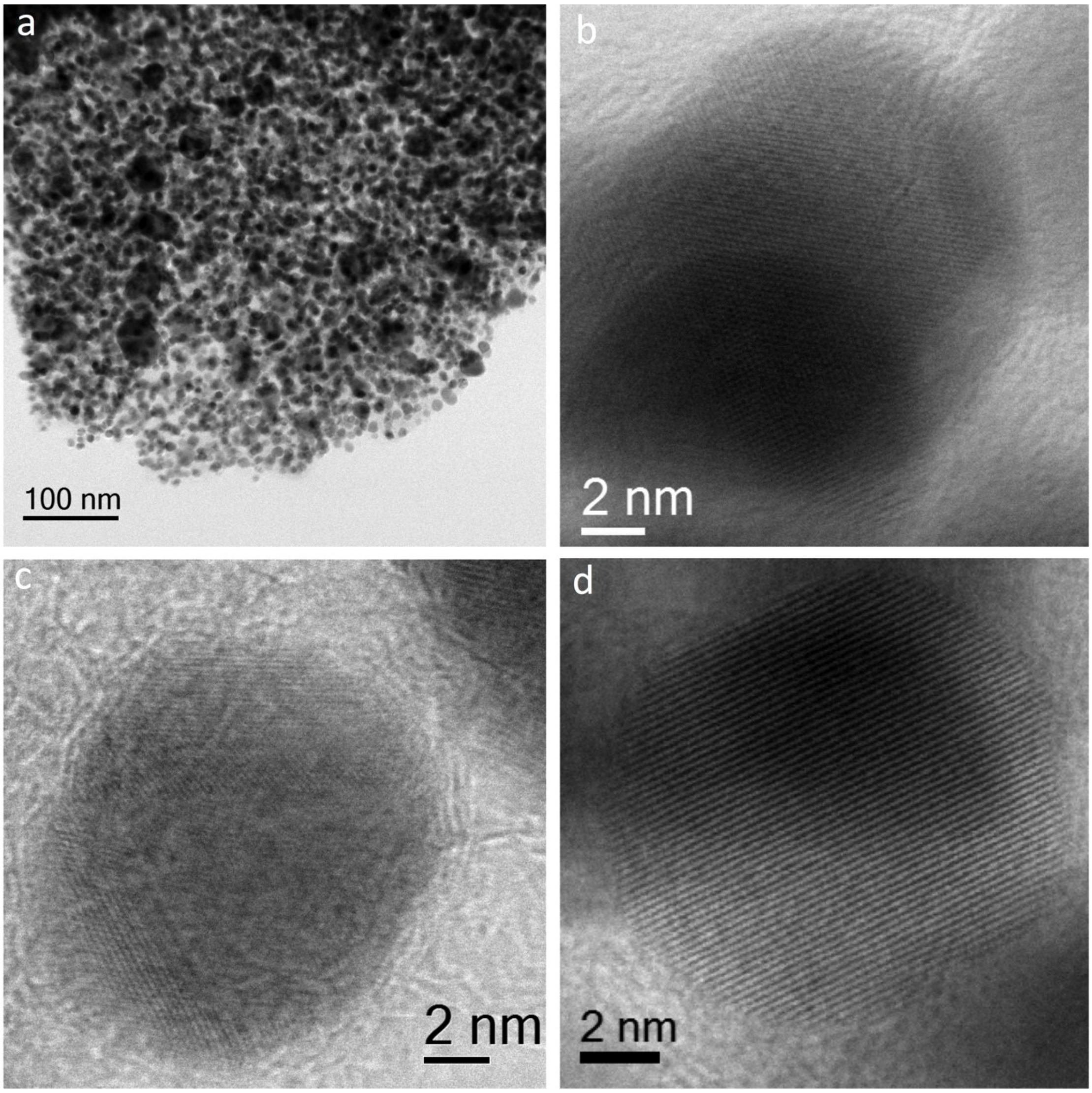

Figure S 14. (a) STEM image of the Ni/C composite scratched off from the Ni-F substrate. (b-d) STEM images of the Ni/C composite under higher magnifications. These STEM inspections clearly reveal the fact that no Ni/NiO heterostructures can be observed in the Ni/C composite, as no boundaries can be detected within the nanoparticles.

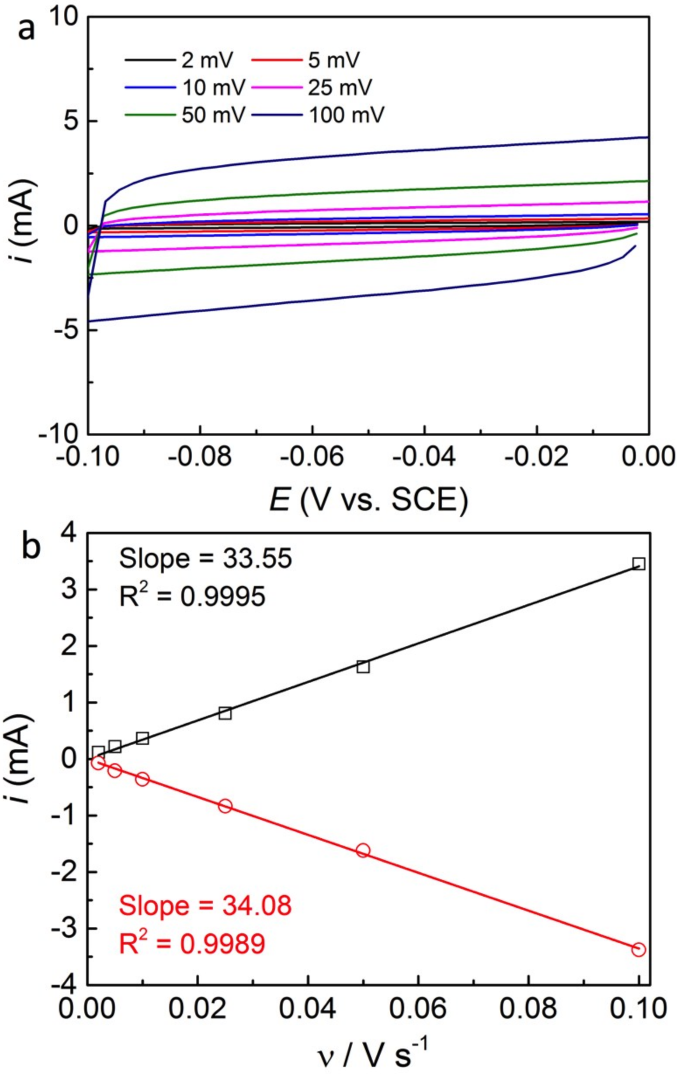

Figure S 15. Charging currents measured in the non-Faradaic potential range at scan rates of 2, 5, 10, 25, 50 and 100 mV s^{-1} with the Mn-NiO-Ni/Ni-F electrode in 1 M KOH solution. Figure b represents the cathodic (red circle) and anodic (black square) charging currents measured at -0.05 V vs. SCE with the Mn-NiO-Ni/Ni-F electrode, plotted against the scan rates.

The double-layer capacitance determined from this system is taken by the average of the absolute value of anodic and cathodic slopes of the linear fits. The double layer capacitance (C_{DL}) of the Mn-NiO-Ni/Ni-F electrode measured from the scan rate dependent CVs is 33.81 mF. The electrochemical active surface area (ECAS) of Mn-NiO-Ni/Ni-F is determined to be 845.25 cm^{-2} by adopting a specific capacitance (C_S) value C_S = 0.040 mF cm^{-2}. The geometric surface area (GSA) of the Mn-NiO-Ni/Ni-F electrode used for ECAS measurement is 3 cm^2, therefore a roughness factor of 281 can be obtained herein.

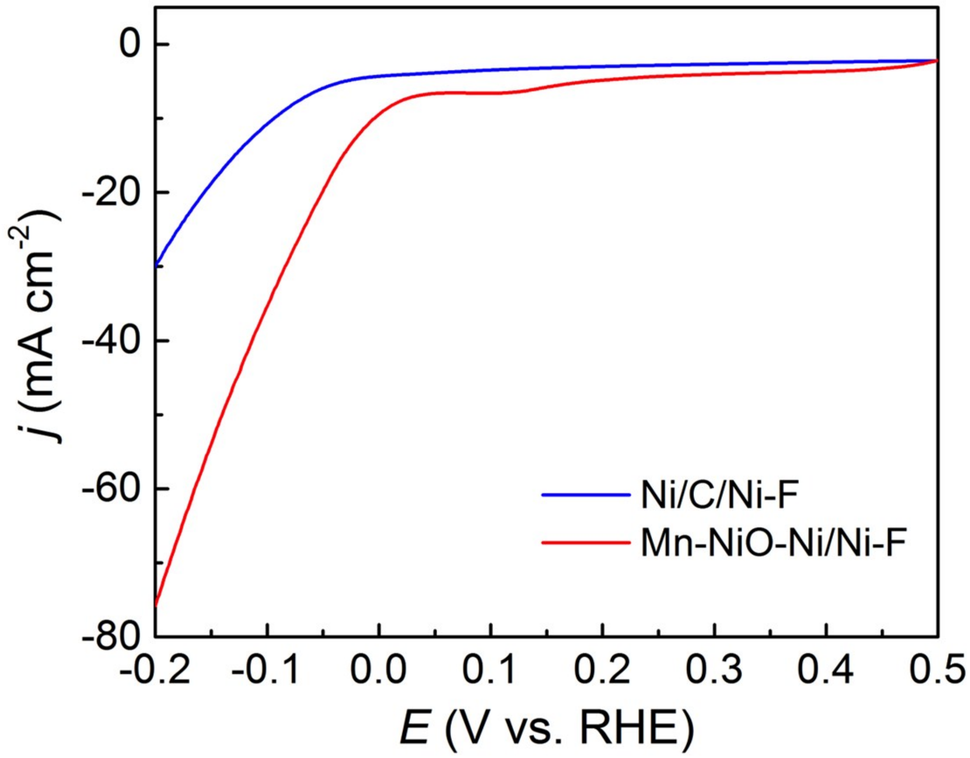

Figure S 16. HER polarization curves obtained with the Ni/C/Ni-F and Mn-NiO-Ni/Ni-F electrode in 1 M KOH at a scan rate of 1 mV s^{-1} without compensating the iR drop.

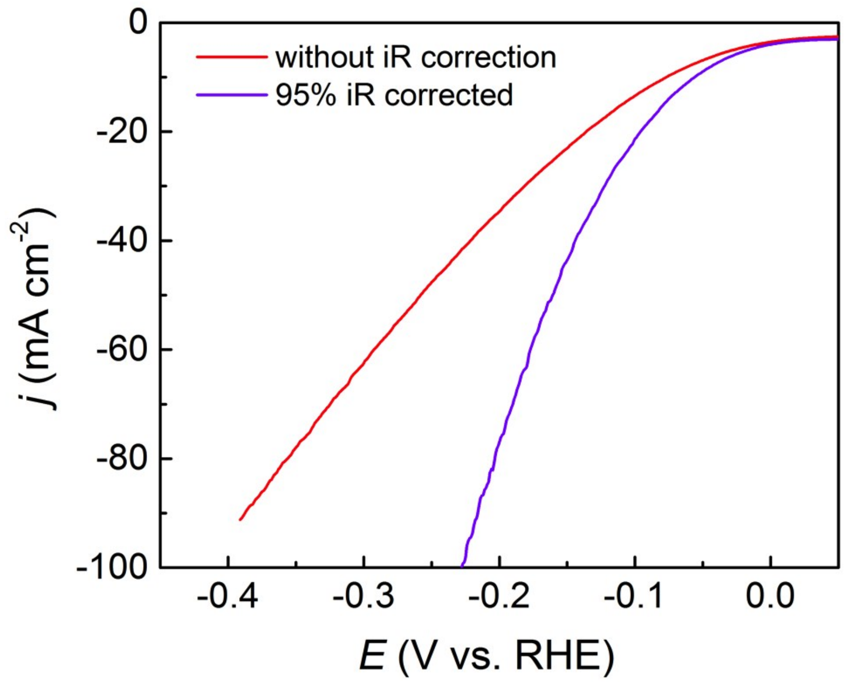

Figure S 17. HER polarization curves obtained with the Mn-NiO-Ni/Ni-F electrode in 1 M PB solution with and without correcting the iR drop. The scan rate is 1 mV s^{-1}.

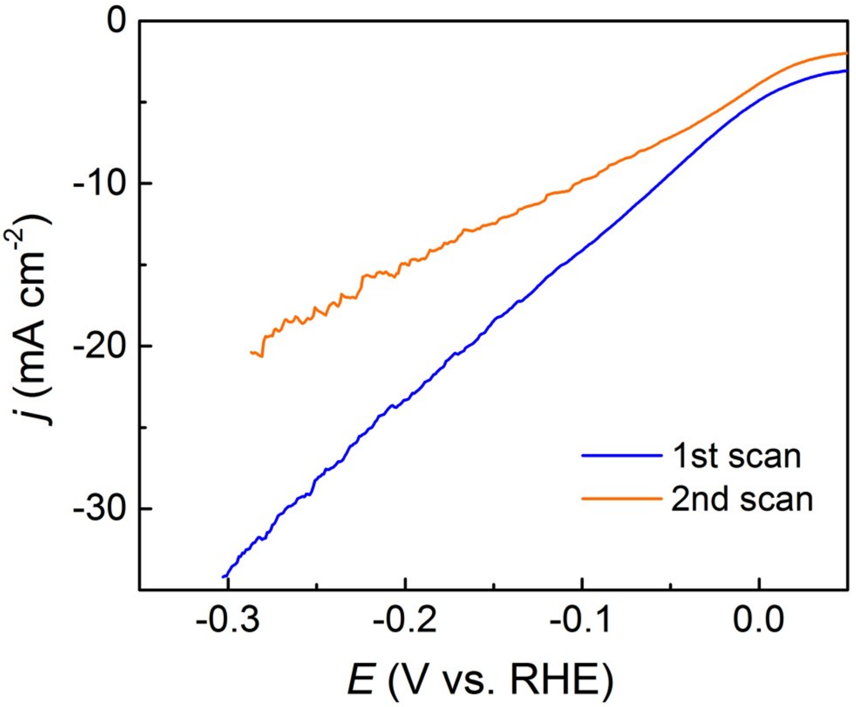

Figure S 18. The instability issue of Pt/C/Ni-F. The first and second HER polarization curves obtained with the Pt/C/Ni-F electrode in 1 M PB solution at 1 mV s^{-1}.

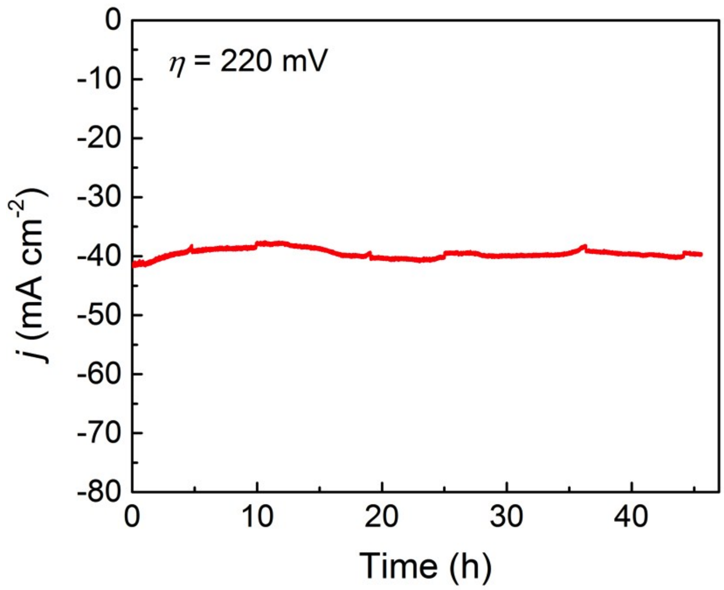

Figure S 19. Chronoamperometric curve obtained with the Mn-NiO-Ni/Ni-F electrode in 1 M PB solution with a constant applied potential of -0.22 V.

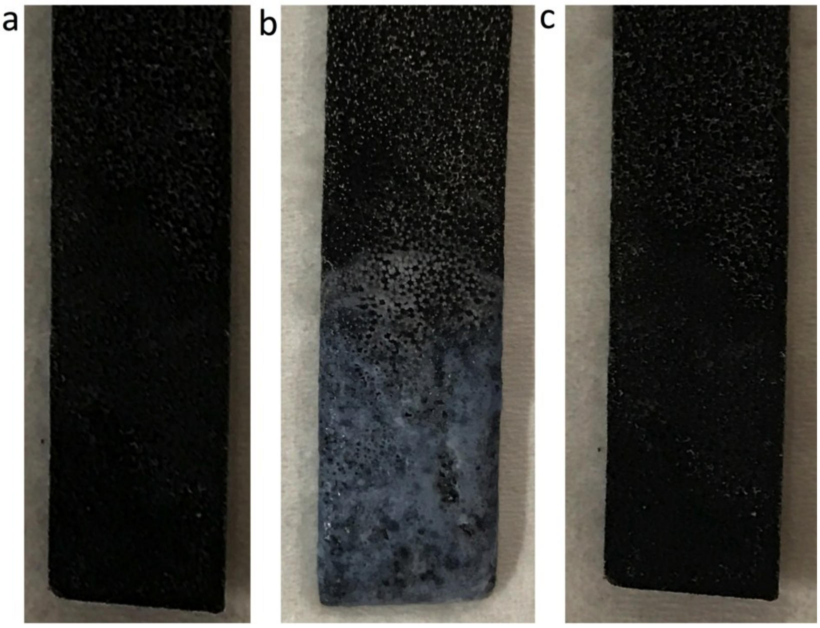

Figure S 20. Photos of the Mn-NiO-Ni/Ni-F electrode (a) before HER in seawater, (b) after 14 h of HER in seawater at -0.14 V and (c) after treatment in acid.

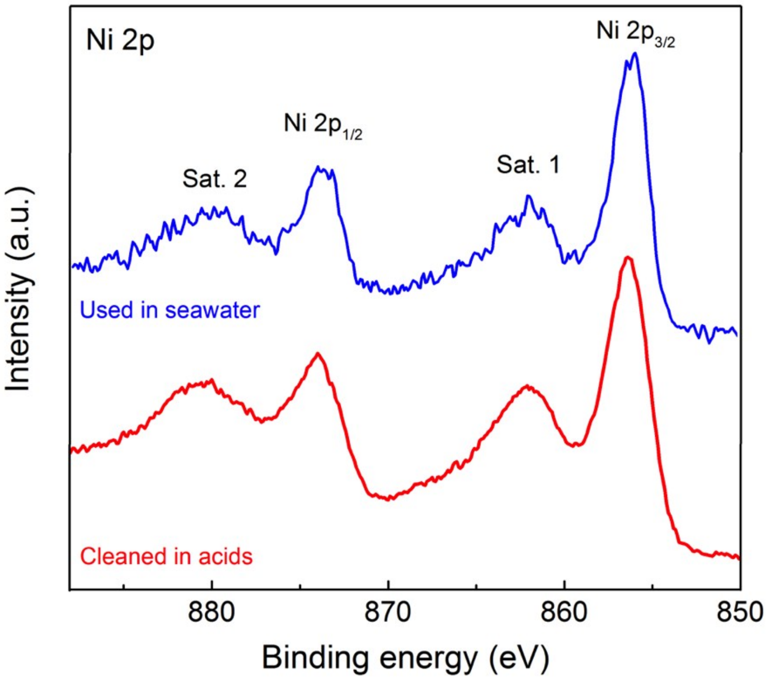

Figure S 21. High resolution XPS Ni 2p spectra of the MnO-NiO-Ni/Ni-F electrode after being used for HER in seawater (blue line) and cleaned in diluted acidic solutions (red line).

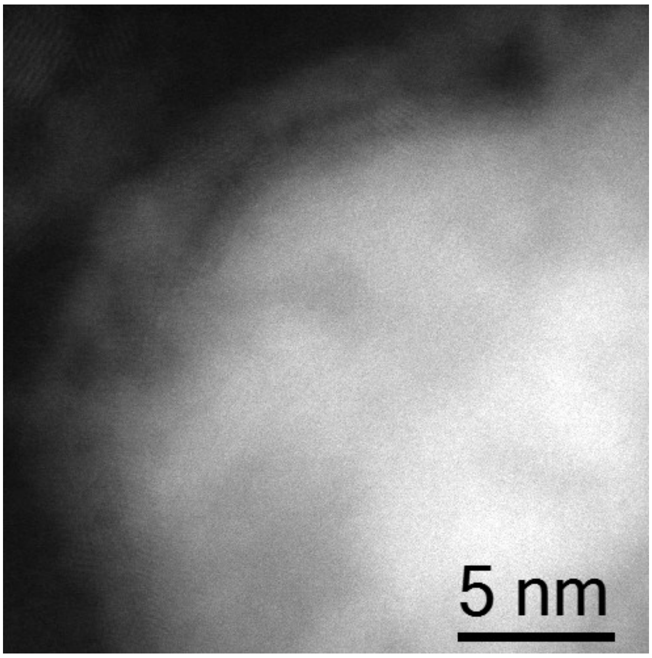

Figure S 22. A high resolution HAADF-STEM image of the Mn-NiO-Ni composite scratched off from the Ni-F. It can be clearly seen in this figure that many voids are existed in the NiO shell, which may allow the exposure of a great amount of adjacent NiO and Ni species.

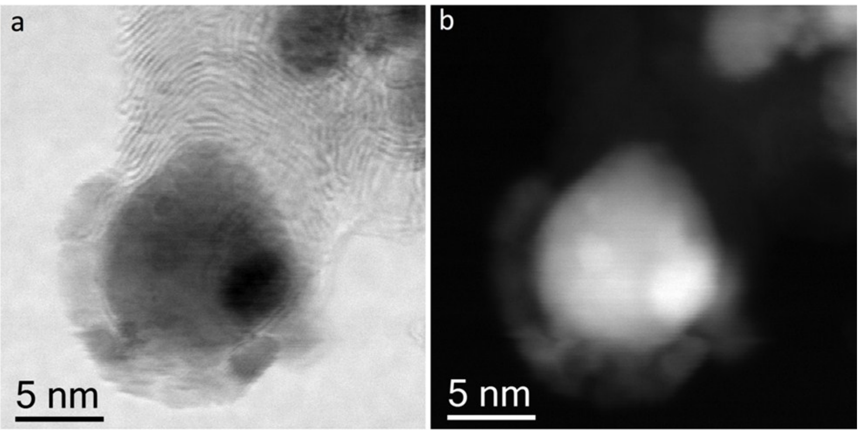

Figure S 23. (a) STEM image of the NiO-Ni composites prepared via the thermal treatment. **(b)** The corresponding HAADF image of **(a)**.

As the formation of NiO-Ni/Ni-F composites were not achievable in the absence of the Mn-MOF, an alternative method of synthesizing Ni/NiO heterostructures was utilized for comparative purposes. Ni-C composites were prepared via hydrothermal treatment of nickel acetate tetrahydrate and 2,5-dihydroxyterephthalic acid dissolved in tetrahydrofuran for 72 h at 383 K. The obtained powder was washed with water and ethanol and dried prior to calcination in Ar at 773 K for 2 h and then 973 K for 3 h. The sample was then controllably oxidized in a flow through reactor system with 100 mg of sample being heated in air to 523 K for 2 h to obtain a Ni/NiO composite in the absence of Mn. Figure S 23 shows the STEM and the corresponding HAADF images of the NiO-Ni composite obtained from the thermal treatment. It can be clearly seen from these images that a Ni/NiO core-shell structure was obtained. The electrode was prepared via drop-casting the NiO-Ni catalyst ink onto Ni-F. Figure S24 represents the HER polarization curves obtained with the NiO-Ni/Ni-F and Mn-NiO-Ni/Ni-F electrodes in seawater. It can be seen from Figure S 28 that Mn-NiO-Ni/Ni-F exhibited far better HER catalytic activity than the NiO-Ni/Ni-F electrode in seawater, showing lower onset overpotential (50 mV compared with 200 mV of NiO-Ni/Ni-F), and higher current density at any given potentials (35 mA cm^{-2} compared with 15 mA cm^{-2} at -0.4 V). The disparity in catalytic can be ascribed to the structural advantages (free-standing electrode, well-aligned catalyst arrays) as well as the presence of Mn element in the Mn-NiO-Ni/Ni-F electrode.

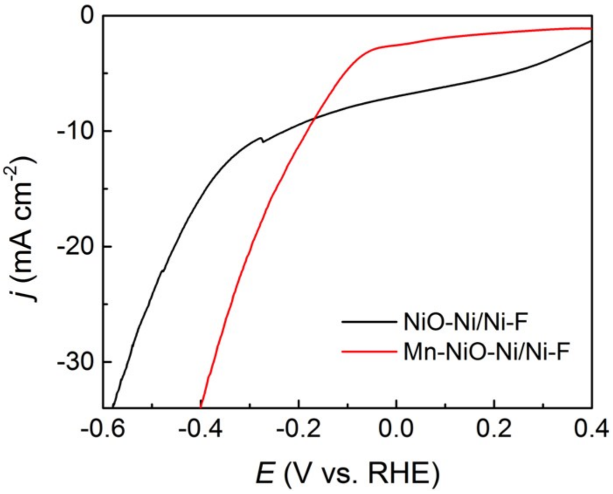

Figure S 24. HER polarization curves obtained with the NiO-Ni/Ni-F and Mn-NiO-Ni/Ni-F electrodes in natural seawater at 1 mV s^{-1}. The loading of NiO-Ni on Ni-F was 0.5 mg cm^{-2}.

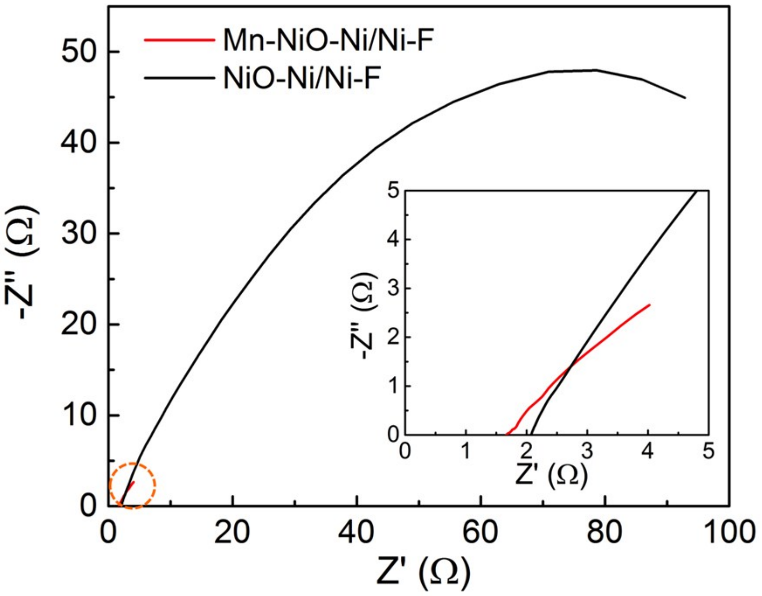

Figure S 25. EIS spectra of the Mn-NiO-Ni/Ni-F and NiO-Ni/Ni-F electrodes measured in 1 M KOH with an applied overpotential of 50 mV. Inset is the enlarged figure of the area marked with the orange circle. The EIS measurements were carried out by applying an AC voltage with 5 mV amplitude in a frequency range from 100000 to 1 Hz.

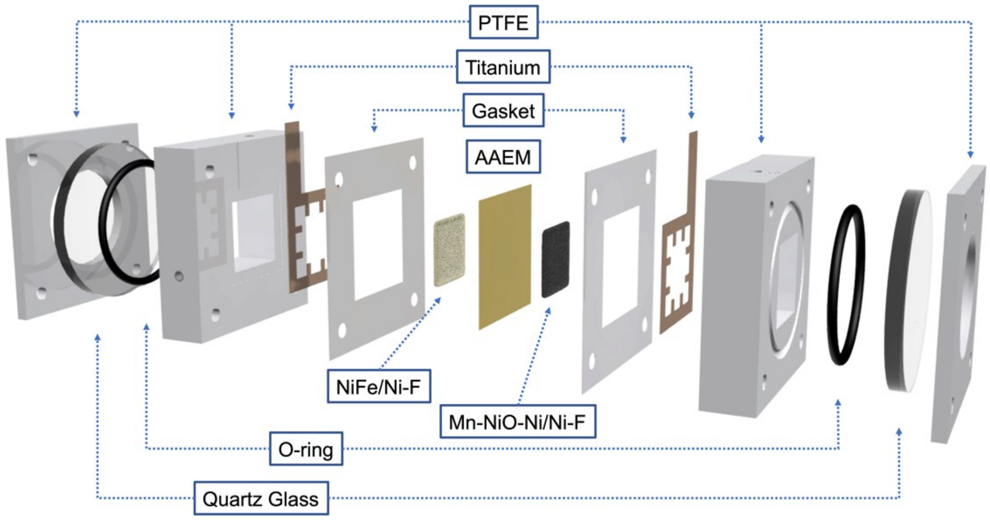

Figure S 26. Schematic illustration of the customized water electrolyzer cell.

The cell built was a two-electrode water electrolysis system with PTFE body. The cathode and anode was separated by an alkaline anion exchange membrane (AAEM) (FUMASEP® FAA-3-PK-75). This customized electrolyzer cell allows the adoption of 3D electrodes (e.g. Ni-F) without damaging the structure, as opposed to conventional designs. The Mn-NiO-Ni/Ni-F electrode was adopted as the cathode and a NiFe/Ni-F electrode was used as the anode. The bubbles evolved in this cell can be easily visualized via two quartz glass windows introduced on each side (also refer to the photo show in Figure S26). 1 M KOH was employed as the electrolyte in this cell so as to maximize the catalytic activity of the NiFe/Ni-F anode.

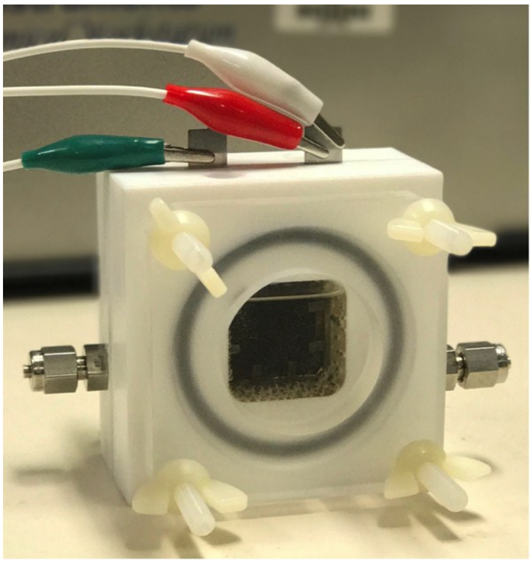

Figure S 27. Photo of the customized water electrolyzer cell. With the presence of quartz glass windows, the bubble evolution during water splitting can be easily monitored.

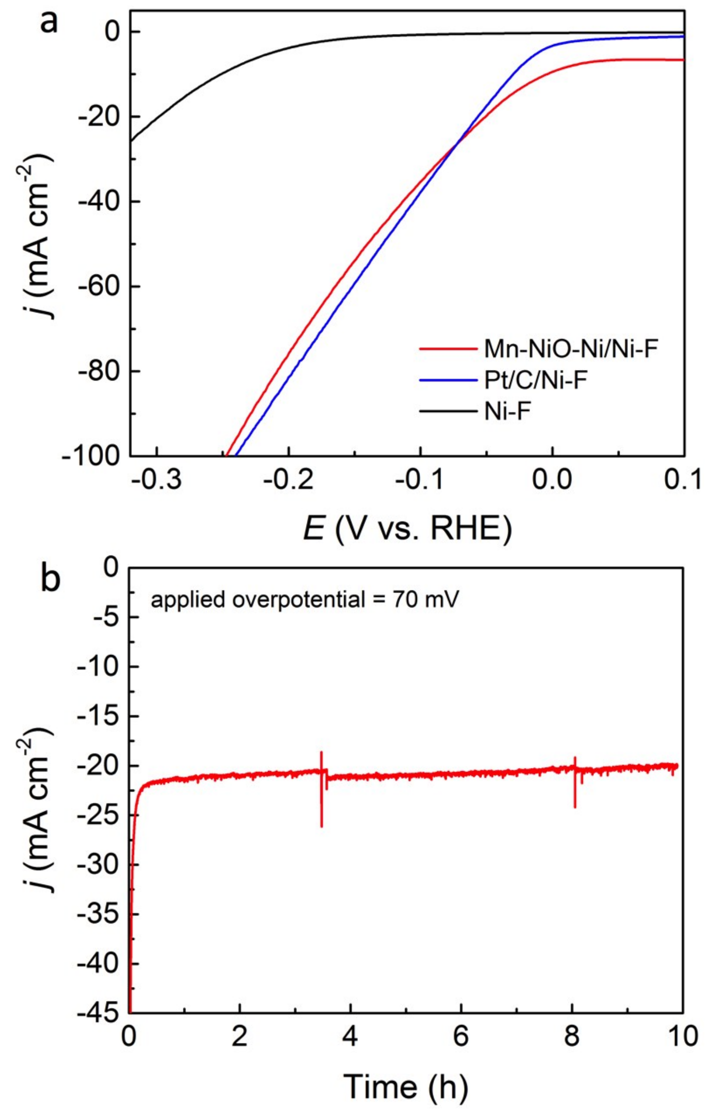

Figure S 28. (a) HER polarization curves obtained with the Mn-NiO-Ni/Ni-F, Pt/C/Ni-F, and bare Ni-F electrodes in 1 M KOH solution at 1 mV s^{-1}. (b) A chronoamperometric curve obtained with the Mn-NiO-Ni/Ni-F electrode in 1 M KOH solution with a constant applied potential of -0.07 V.

Figure S28 exhibits the HER performances of the Mn-NiO-Ni/Ni-F electrode in 1 M KOH. Due to the higher conductivity as well as the presence of higher quantities of hydroxide ions, the Mn-NiO-Ni/Ni-F displays higher activity in 1 M KOH than in both 1 M PB solution and seawater. The electrode exhibited ~ 0 mV of onset η, and η as low as 10 mV and 248 mV to afford j of 10 and 100 mA cm^{-2}, respectively. Further, the electrode exhibited impressive stability for HER (Figure S28b), with almost unchanged j obtained at -0.07 V for 10 h.

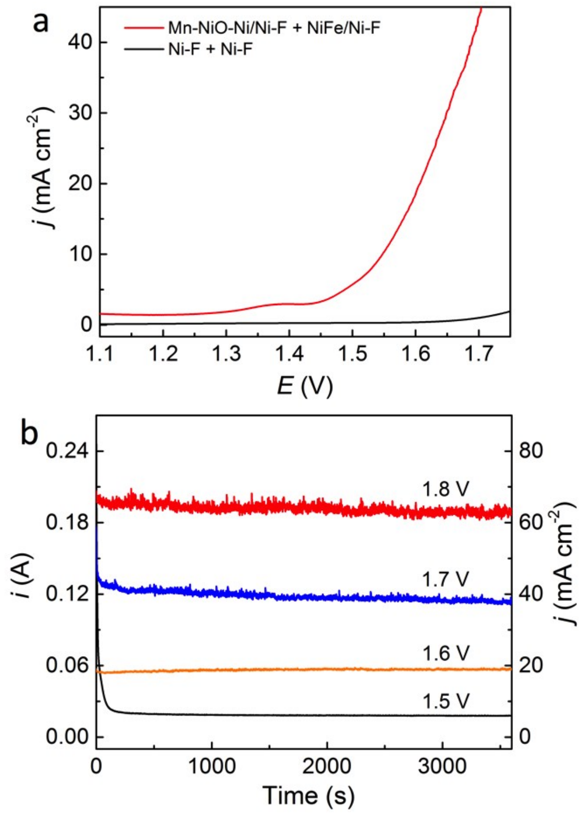

Figure S 29. (a) The two-electrode polarization curve obtained with the electrolyzer cell. The polarization curve obtained with cell using Ni-F as both the cathode and anode is adopted for the comparison purpose. The scan rate is 1 mV s^{-1}. (b) Chronoamperometric curves obtained with the electrolyzer cell at different applied potentials.

The polarization curve in 1 M KOH using the customized cell employing Mn-NiO-Ni/Ni-F as the cathode and NiFe/Ni-F as the anode is shown in Figure S26a. The effective surface area of the cell was 3 cm^2. Even in the two-electrode configuration, the cell is highly active for water splitting, showing an onset potential as low as 1.43 V, corresponding to an overall cell η of merely 200 mV. The j increased rapidly as the increment of applied potential, reaching over 40 mA cm^{-2} at 1.7 V. The polarization curve obtained with Ni-F as both the cathode and anode, for comparison, showed negligible catalytic activity during the same potential range (Figure S25a), indicating the activity is originated from the catalyst materials deposited on Ni-F, rather than the Ni-F substrates. Figure S26b shows the current-time responses of the cell under different applied potentials. Stable currents at ~0.022 A, 0.055 A, 0.12 A and 0.2 A were obtained at 1.5 V, 1.6 V, 1.7 V and 1.8 V, respectively.

Figure S 30. Photo of the solar panel-powered water electrolyzer cell.

In this experiment, a solar panel (FuelCellStore, Texas) was adopted as the source of electricity to power the customized water electrlyzer cell. The output voltage of this solar panel was measured ~ 1.8 V under our testing conditions. Vigorous bubble evolution can be visualized within the electrolyzer cell upon the illumination of sunlight.

Table S 1. Comparisons of HER catalytic activities of the Mn-NiO-Ni/Ni-F electrode with other reported catalysts in neutral electrolytes ([a]Performances were obtained without i*R* correction, [b]Current density = 2 mA cm^{-2})

Catalyst	**Catalyst amount (mg cm^{-2})**	**Electrolyte**	**Onset η**	**η at j = 10 mA cm^{-2}**	**Ref**
Mn-NiO-Ni/Ni-F[a]	0.25	1 M PB solution (pH = 7)	~0 mV	80 mV	This work
Co NPs@N-CNTs[a]	0.28	1 M PB solution (pH = 7)	250 mV	540 mV	S1
Cu_2MoS_4[a]	0.04	0.1 PB solution (pH = 7)	~ 550 mV	~ 750 mV	S2
Co-S	N.A.	1 M PB solution (pH = 7)	43 mV	170 mV	S3
Co-B	N.A.	0.5 M PB solution (pH = 7)	70 mV	251 mV	S4
Ni-Mo-S	0.52	0.5 M PB solution (pH = 6.9)	~132 mV	200 mV	S5
CoNx/C	2.0	1 M PB solution (pH =7)	30 mV	247 mV	S6
FeP	1.0	1 M PB solution (pH = 7)	~ 20 mV	102 mV	S7
S-$NiFe_2O_4$/NF	N.A.	1 M PB solution (pH = 7.4)	~120 mV	197 mV	S8
NiS_2/MoS_2	0.2	0.1 M PB solution (pH = 7)	200 mV	284 mV	S9
CoP_3 HSs	1	1 M PB solution (pH = 7)	100 mV	168 mV	S10
$Zn_{0.3}Co_{2.7}S_4$	0.285	0.1 M PB solution (pH = 7)	~ 50 mV	90 mV	S11
CoP/CC[a]	N.A.	1 M PB solution (pH = 7)	45 mV	~ 110 mV	S12
H_2-CoCat/FTO	N.A.	1 M PB solution (pH = 7)	50 mV	385 mV[b]	S13
Mo_2C@NC	~ 0.28	0.1 M PB solution (pH = 7)	~ 40 mV	156 mV	S14
MoP/Mo_2C@C	0.453	1 M PB solution (pH = 7)	60 mV	136 mV	S15

References

S1. Zou, X. X. *et al.* Cobalt-Embedded Nitrogen-Rich Carbon Nanotubes Efficiently Catalyze Hydrogen Evolution Reaction at All pH Values**. *Angew Chem Int Edit* **53**, 4372-4376 (2014).

S2. Tran, P. D. *et al.* Copper molybdenum sulfide: a new efficient electrocatalyst for hydrogen production from water. *Energ Environ Sci* **5**, 8912-8916 (2012).

S3. Sun, Y. J. *et al.* Electrodeposited Cobalt-Sulfide Catalyst for Electrochemical and Photoelectrochemical Hydrogen Generation from Water. *J Am Chem Soc* **135**, 17699-17702 (2013).

S4. Gupta, S., Patel, N., Miotello, A. & Kothari, D. C. Cobalt-Boride: An efficient and robust electrocatalyst for Hydrogen Evolution Reaction. *J Power Sources* **279**, 620-625 (2015).

S5. Miao, J. W. *et al.* Hierarchical Ni-Mo-S nanosheets on carbon fiber cloth: A flexible electrode for efficient hydrogen generation in neutral electrolyte. *Science Advances* **1** (2015).

S6. Liang, H. W. *et al.* Molecular metal-N-x centres in porous carbon for electrocatalytic hydrogen evolution. *Nat Commun* **6** (2015).

S7. Callejas, J. F. *et al.* Electrocatalytic and Photocatalytic Hydrogen Production from Acidic and Neutral-pH Aqueous Solutions Using Iron Phosphide Nanoparticles. *Acs Nano* **8**, 11101-11107 (2014).

S8. Liu, J., Zhu, D., Ling, T., Vasileff, A. & Qiao, S.-Z. S-NiFe2O4 ultra-small nanoparticle built nanosheets for efficient water splitting in alkaline and neutral pH. *Nano Energy* **40**, 264-273, doi:https://doi.org/10.1016/j.nanoen.2017.08.031 (2017).

S9. Kuang, P. Y., Tong, T., Fan, K. & Yu, J. G. In Situ Fabrication of Ni-Mo Bimetal Sulfide Hybrid as an Efficient Electrocatalyst for Hydrogen Evolution over a Wide pH Range. *Acs Catal* **7**, 6179-6187 (2017).

S10. Wu, T. *et al.* Hierarchical cobalt poly-phosphide hollow spheres as highly active and stable electrocatalysts for hydrogen evolution over a wide pH range. *Appl Surf Sci* **427**, 800-806, doi:https://doi.org/10.1016/j.apsusc.2017.08.154 (2018).

S11. Huang, Z. F. *et al.* Hollow Cobalt-Based Bimetallic Sulfide Polyhedra for Efficient All-pH-Value Electrochemical and Photocatalytic Hydrogen Evolution. *J Am Chem Soc* **138**, 1359-1365 (2016).

S12. Tian, J. Q., Liu, Q., Asiri, A. M. & Sun, X. P. Self-Supported Nanoporous Cobalt Phosphide Nanowire Arrays: An Efficient 3D Hydrogen-Evolving Cathode over the Wide Range of pH 0-14. *J Am Chem Soc* **136**, 7587-7590 (2014).

S13. Cobo, S. *et al.* A Janus cobalt-based catalytic material for electro-splitting of water. *Nat Mater* **11**, 802-807 (2012).

S14. Liu, Y. P. *et al.* Coupling Mo2C with Nitrogen-Rich Nanocarbon Leads to Efficient Hydrogen-Evolution Electrocatalytic Sites. *Angew Chem Int Edit* **54**, 10752-+ (2015).

S15. Zhang, L. N. *et al.* MoP/Mo2C@C: A New Combination of Electrocatalysts for Highly Efficient Hydrogen Evolution over the Entire pH Range. *Acs Appl Mater Inter* **9**, 16270-16279 (2017).